Application of the view factor model on the particle-in-cell and Monte Carlo collision code

Ruojian Pan,[1] Junxue Ren,[2] Haibin Tang,[1,3,4,*] Shuai Cao,[2] Juan Li,[5] Zhe Zhang,[6] Jun Zhou,[2] and Jinbin Cao[1,4]

[1]*School of Space and Environment, Beihang University, Beijing 100083, China*

[2]*School of Astronautics, Beihang University, Beijing 100083, China*

[3]*Key Laboratory of Spacecraft Design Optimization and Dynamic Simulation Technologies, Ministry of Education, Beijing 100083, China*

[4]*Laboratory of Space Environment monitoring and Information Processing, Ministry of Industry and Information Technology, Beijing 100083, China*

[5]*National Key Laboratory of Science and Technology on Vacuum Technology & Physics, Lanzhou Institute of Physics, Lanzhou 730000, China*

[6]*School of Instrumentation and Optoelectronic Engineering, Beihang University, Beijing 100083, China*

(Received 7 March 2019; revised 2 April 2020; accepted 3 August 2020; published 16 September 2020)

Particle-in-cell and Monte Carlo collision (PIC-MCC) has been widely adopted as a simulation method for electric propulsion. However, neutral atoms move much more slowly than other species, which can cause a serious reduction in simulation speed. In this work, we investigate the view factor model in combination with the PIC-MCC method and propose a method for simulating three-dimensional neutral atoms. The accuracy of the PIC-MCC method can be significantly improved by updating the neutral distribution periodically. We compare the computational results with the fixed-neutral PIC-MCC model of the miniature ring-cusp discharge experiment at the University of California, Los Angeles (UCLA). The plasma distribution and potential distribution of the simulation match well with the UCLA experimental data. Compared with the fixed-neutral model, the view factor model increases the simulation time by only 33% while it improves the distribution accuracy of neutrals, plasma density, and electric potential, and reduces the simulation errors of discharge current and discharge power from 19.8% to 9.8%. The accuracy of PIC-MCC simulation has been improved at the expense of slightly increasing the computational time.

DOI: 10.1103/PhysRevE.102.033311

I. INTRODUCTION

Electric propulsion (EP) has been used for many small satellites and nanosatellites in the past few decades [1,2]. Numerical simulation is a good approach for researchers to learn the physical and working processes of EP systems. As the key aspect of EP studies is to investigate the plasma, the EP simulation is normally done in one of three ways, including the full particle method, the hybrid particle method, and the fluid method [3]. Among these methods, because it treats all the species (including neutrals, ions, and electrons) as particles and has the most minimal physical assumptions, the full particle method is the easiest way for researchers to develop an understanding of the actual physical mechanisms. Thus, the full particle method is not only used in the simulation of EP [4–6] but also widely used to simulate plasmas in other fields, for example, laser plasma [7], the interactions of particles and plasma [8], extreme ultraviolet radiation driven plasma [9], etc.

However, it is too computationally expensive to simulate EP with the full particle method, for two main reasons. The first is that tracking all kinds of species as particles would increase the computational load dramatically. Using the full particle-in-cell and Monte Carlo collision (PIC-MCC) method, all the movements and interactive collisions of particles in the EP chamber must be simulated by calculating all individual particles. However, the number density of the particles in EP chambers would usually be at 10^{17}–10^{19} m^{-3}. Three main approaches have been researched to accelerate the simulations, i.e., reducing the mass of heavy particles [3,10], increasing the vacuum permittivity [10,11], and the self-similarity model [12,13]. To simulate different kinds of thrusters, including Hall-effect thrusters [14–16], ion engines [6,17,18], and magnetoplasmadynamic thrusters (MPDTs) [19,20], one or more numerical acceleration methods have been used. When not using parallel computation techniques, numerical acceleration methods are almost unavoidable to calculate the huge number of particles in the high plasma density area (e.g., discharge chamber and hollow cathode internal structure). These methods have been proved to be effective to reduce the computational time but have some effects on the accuracy of the physical results. Increasing the vacuum permittivity would cause a thicker sheath near the chamber walls. Furthermore, reducing the mass of heavy particles would result in a relatively lower density distribution of plasma in the chamber. This paper also uses moderate numerical acceleration methods to reduce the computational time; they are described in detail in the Simulation section. However, what we investigate herein is the bulk plasma region but not the sheaths, and the same numerical acceleration methods or computational environments are used in all cases. Thus, our main conclusions would still hold if the numerical acceleration methods were not used.

The second reason is that treating the neutrals like ions or electrons as particles can greatly increase the simulation

*Corresponding author: thb@buaa.edu.cn

time. As the time step for the PIC-MCC method depends on the electron characteristic time ($\sim 10^{-11}$ s) and the real time for the particles to be steady is at the magnitude of 10^{-5}–10^{-4} s, total time steps can be at the magnitude of 10^6 or higher to simulate an EP device using the full PIC method. Previous studies have used direct simulation Monte Carlo (DSMC) [5,21,22] to simulate neutrals directly, or the original PIC-MCC [3,23] method where neutrals are tracked in the same way as ions and electrons. For serial computations, running with this type of full PIC method takes several weeks or months even if numerical acceleration methods are used. The reason is that the neutrals move much more slowly than the ions and electrons which are pushed by the electric fields. The slow speed causes a slow convergence, delaying the entire simulation which converges only once all the species reach steady states. To reduce the simulation time, researchers have adopted different approaches to calculate the neutrals. The neutral distribution change is much smaller and slower than the change of ions and electrons, so Mahalingam *et al.* applied a fixed-neutral model [6,24] to avoid the high computational cost of the neutrals. In this method, neutral change was assumed to be neglected so that the neutral distribution has been set to be uniform in the discharge chamber or to be a constant background distribution simulated by a lower gas flow rate [25]. The fixed-neutral model has great advantages for the computational speed and has been successfully applied to the PIC modeling of ion thrusters [26], Hall-effect thrusters [5,14], and hollow cathodes [27]. This can result in a fast simulation and provide a great deal of thruster information. However, changes in neutral distribution would undoubtedly influence the physical process and simulation accuracy. Adam *et al.* developed a fluid [28] method for simulation of the neutral distribution change to combine with the PIC-MCC code. This is a one-dimensional (1D) model, where the neutral distribution only changes in the axial direction. The fluid model updates the new neutral distribution during every PIC iteration by solving a differential equation. All of the parameters in the equation (discharge frequency, neutral speed, recombination speed) are determined by the PIC-MCC code. This model updates the neutral distribution via a hybrid way to improve the accuracy and has been used in Hall thruster simulation [29]. However, a 1D model is still too simplified for the real physical situation.

A new method, the view factor model, has been proposed in recent years. The view factor model has already been used for thermal radiation simulation and generalized into neutral distribution calculation due to its fast calculation speed. Compared to the MCC and DSMC methods, the view factor model only needs geometry factors and ionization parameters to solve the neutral distribution. Thus, the calculation cost is small and relatively constant because of the fixed calculation progress. Compared with the methods proposed by Mahalingam *et al.* and Adam *et al.*, the view factor model can provide a three-dimensional (3D) treatment of the neutral distribution, resulting in more detailed neutral information. Araki *et al.* used the view factor model in the hybrid TURF code to analyze the sensitivity of the ion flux to the neutral density of the Hall thruster plume but did not take ionization into account [30]. Katz and Mikellides established a whole fluid model combined with the view factor model to calculate the neutrals distribution [31]. Wirz and co-workers at UCLA used the view factor model as a submodel in their lab's code by receiving and sending messages from and to other submodels to simulate the ion thrusters [32,33]. The view factor model has the potential to be a fast and accurate way to calculate neutrals, while the PIC-MCC method has a high degree of accuracy but a slow computational speed when simulating neutrals as particles. However, there has been little research concentrating on the combination of the view factor model with the PIC-MCC method, which might provide a both fast and accurate method for the EP simulation.

In this paper, to discuss the feasibility of combining the view factor model with the PIC-MCC code, we analyze the PIC-MCC simulation algorithm and the required parameters of the view factor model to calculate the neutral distribution. A view factor model, which is suitable for combination with the PIC-MCC code, is established and integrated into the PIC codes. We simulate the charged species, the electrons, and ions, with the PIC-MCC code and update the neutral distribution periodically using the view factor model. For the view factor model solution, the geometry factors can be initially determined and the ionization parameters can be determined from the PIC-MCC method. Results from the full PIC code and the COMSOL package are used to verify the accuracy of the view factor model. To test the accuracy improvement of our model, we simulate the UCLA miniature ring-cusp discharge device [34,35] and compare against the simulation results using the Mahalingam fixed-neutral model which assumes a constant neutral distribution [25]. The differences in the results and the convergence time are analyzed and discussed in detail.

II. METHOD

A. Brief introduction to the PIC-MCC code

The JLPP2.5 code is a complete model developed by Joint Laboratory of Plasma & Propulsion (JLPP) in Beihang University. Two simulation models have been developed and

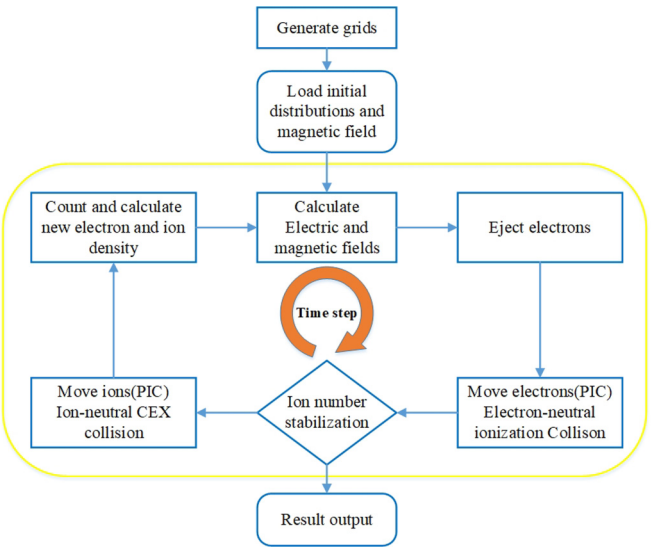

FIG. 1. The scheme of the numerical algorithm of particle-in-cell and Monte Carlo collision.

TABLE I. Different particle and collision types in our PIC-MCC code, which include the collisions between neutrals and electrons, ions (primary and secondary) and electrons, and between ions and neutrals.

Particle type	Collision type
$Xe+e^-$	Elastic collision $Xe+e^- \rightarrow Xe+e^-$ Excitation collision $Xe+e^- \rightarrow Xe^*+e^-$ Ionization collision $Xe+e^- \rightarrow Xe^+ +2e^-$
$Xe^+ +e^-$	Excitation collision $Xe^+ +e^- \rightarrow Xe^{+*}+e^-$ Ionization collision $Xe^+ +e^- \rightarrow Xe^{++}+2e^-$ Compound collision $Xe^+ +2e^- \rightarrow Xe+e^-$
$Xe^{++}+e^-$	Excitation collision $Xe^{++}+e^- \rightarrow Xe^{+++*}+e^-$ Compound collision $Xe^{++}+2e^- \rightarrow Xe^+ +e^-$
$Xe^+ +Xe$ $Xe^{++}+Xe$ (Xe^+, for example)	Elastic collision $Xe^+ +Xe \rightarrow Xe^+ +Xe$ Charge-exchange collision $Xe^+ +Xe \rightarrow Xe + Xe^+$

there are no differences between these two methods except for the treatment of the neutrals. One method consists in treating the neutrals as particles, while the other fixes the neutrals as a background distribution to achieve a high-speed calculation. The code has been successfully used for several papers, including researching the magnetic mirror effect in a Hall-effect thruster [14], the energy deposition on a hollow cathode [27,36], the magnetic fields at the exit of a magnetoplasmadynamic thruster (MPDT) [20], and other physical effects in MPDT [37,38].

JLPP2.5 is a 2.5D axisymmetric PIC-MCC system used in EP simulation. It divides the EP thrusters' axisymmetric plane into finite grids and updates the particle movements and electric field during each time step. There are four main compound procedures in each step: (1) using particle density parameters to solve the Poisson equation and getting the newly updated electric field; (2) injecting the particles into the EP discharge chamber and calculating the movement driven by the electromagnetic field; (3) using the MCC method to simulate the collisions between particles; (4) calculating the density of the new particles on the nodes. If different particle densities are all convergent after the iterations, the PIC-MCC code exits the loop and outputs the results. The schematic of the PIC-MCC numerical algorithm is shown in Fig. 1.

The collision types in procedure (3) are shown in Table I. Furthermore, in order to reduce the calculation load, we adopt the null collision method to avoid searching all information of particles in a time step [21,39].

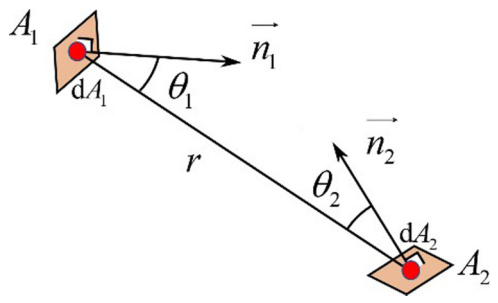

FIG. 2. The view factor of two finite surfaces (A_1 to A_2).

B. View factor model

View factor is a geometry factor and a concept in heat transfer theory, which has been frequently used in thermal radiation calculations [40,41]. For two diffusing faces a and b which are isothermal and have uniform physical properties, the radiation incident on surface b coming from surface a is defined as $R_{a\rightarrow b}$, while the total effective radiation of surface b from all surfaces is defined as $R_{b,\mathrm{all}}$. Thus, the definition of thermal view factor Ψ_{ab} is

$$\Psi_{ab} = \frac{R_{a\rightarrow b}}{R_{b,\mathrm{all}}}. \tag{1}$$

For two finite surfaces (Fig. 2), $\Psi_{A_1A_2}$ is calculated in the integral form as given by Eq. (2). dA refers to the differential parts of a surface A and $\vec{n}$ refers to the normal vector of each differential surface.

$$\Psi_{A_1A_2} = \frac{1}{A_1}\int_{A_1}\int_{A_2}\frac{\cos\theta_1\cos\theta_2}{\pi r^2}dA_1dA_2. \tag{2}$$

Two types of view factor are calculated in this paper. First, for a differential surface, dA_1 and a finite surface A_2 (Fig. 3), $\Psi_{dA_1A_2}$ is used to determine the view factor between two wall elements. dA_1 is a differential surface at the center of the unit sphere. A_s is the projection area of a finite surface A_2 on the sphere and $A_{s,p}$ is the projection of A_s on the bottom plane.

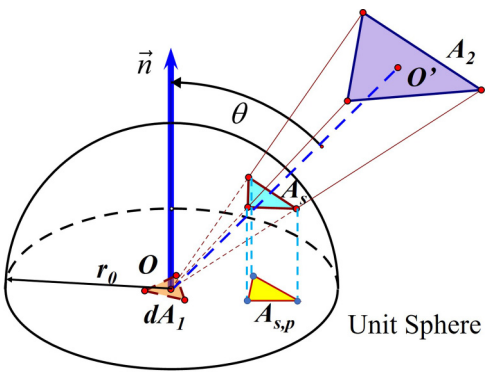

FIG. 3. The view factor of a differential surface dA_1 to a finite surface A_2.

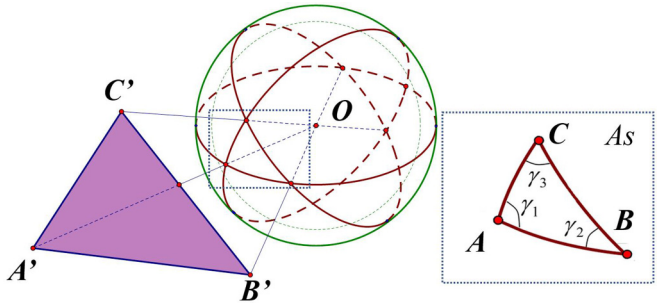

FIG. 4. The view factor of a differential (or finite) surface to a point.

θ is the angle between the normal vector **n** and OO', which changes relatively little and is treated as a constant. $\Psi_{dA_1A_2}$ is calculated by the Nusselt analog [42], as given by Eq. (3).

$$\Psi_{dA_1A_2} = \frac{1}{\pi r_0^2}\int_{A_{s,p}} dA_{s,p} = \frac{1}{\pi r_0^2}\int_{A_s} \cos(\theta) dA_S = \frac{A_s}{\pi}\cos(\theta). \tag{3}$$

Second, for a differential (or finite) surface and a point (Fig. 4), Ψ_{AO} is used to determine the view factor of wall elements to inner nodes. O is the center of the unit sphere. A_s is the projection area of the finite surface A on the unit sphere, which is calculated by three spherical angles, $\gamma_1, \gamma_2, \gamma_3$. The calculation of the spherical angle would use non-Euclidean mathematics which solves the problems for the sphere geometry. Ψ_{AO} is calculated in Eqs. (4) and (5).

$$\Psi_{\mathrm{AO}} = \frac{A_s}{A_{\mathrm{sphere}}} = \frac{A_s}{4\pi}, \tag{4}$$

$$A_s = \gamma_1 + \gamma_2 + \gamma_3 - \pi. \tag{5}$$

For a typical EP thruster where plasma density varies from 10^{17} to $10^{19}\,\mathrm{m}^{-3}$, the mean free path of a neutral atom for interatomic and charge-exchange collisions is sufficiently long to warrant a collision-free approximation [43]. The view factor can be generalized to determine the steady neutral flux balance [44]; it is feasible to apply it to the PIC-MCC simulation of the EP thrusters. To apply the view factor model to EP simulation, the assumptions are given in the following statements.

(1) Neutrals are added by the gas source (including actual gas sources and the chamber walls reemitting) and the recombination of ions and electrons, while they are consumed only by ionization.

(2) The EP chamber and real gas sources are axisymmetric.

(3) The temperature-based speed of neutrals remains constant due to a uniform wall temperature assumption.

(4) Compared with the recombination on the chamber wall, the recombination in the chamber is ignored.

To determine the neutral atoms lost, we generalize a new view factor V, which is a product of the thermal view factor Ψ, the geometry factor G, and the neutral ionization fraction β as given by Eqs. (6) and (7).

$$V_{mh} = G_{mh}\beta_{mh}\Psi_{mh}, \tag{6}$$

$$G_{mh} = \begin{cases} 0 \text{ (blocked)} \\ 1 \text{ (unblocked)} \end{cases}, \tag{7}$$

where G_{mh} is used to evaluate whether there is a block between two surfaces m and h. β_{mh} is the ratio of the final and initial neutral gas flow. According to assumption (3), β is defined as the ratio between the final neutral density (n_o^f) and the initial neutral density (n_o^i) as given by Eq. (8), as a parameter to determine the ionization rate in the EP chamber.

$$\beta \equiv \frac{n_o^f}{n_o^i}. \tag{8}$$

The neutrals are treated as particles passing through a field of electrons, where the local ionization rate is related to the primary electron ionization rates K_{iz}^p and secondary electron ionization rates K_{iz}^s as given by Eq. (9). β is calculated by integrating the ionization parameters along the neutral flow path.

$$\dot{n}_i = \dot{n}_i^p + \dot{n}_i^s = n_o\left(n_p K_{iz}^p + n_s K_{iz}^s\right), \tag{9}$$

where n_o, n_p, n_s represent the densities of neutrals, primary electrons, and secondary electrons, respectively. Neutral loss rate $\dot{n}_o$ is the negative of ion generation rate $\dot{n}_i$. Therefore by solving the differential equation, β between two surfaces can be integrated as given by Eqs. (10) and (11).

$$n_o^f = n_o^i \exp\left[-\int \left(n_s K_{iz}^s + n_p K_{iz}^p\right) dt\right], \tag{10}$$

$$\beta = \exp\left[-\int \left(n_s K_{iz}^s + n_p K_{iz}^p\right) dt\right]. \tag{11}$$

C. View factor model combining with the PIC-MCC code

The EP chamber structure in the JLPP2.5 code fits well with the conditions where the neutral view factor model can be applied, so we design a view factor model algorithm which is suitable for our PIC-MCC code to calculate and update the neutral distribution in the EP chamber. For coupling the PIC-MCC code and the view factor model, we divide the PIC-MCC simulation regime to fit the view factor model. The view factor model and the PIC-MCC algorithm are, respectively, used to simulate the neutrals and the other particles (ions and electrons). While the neutrals change much slower than the charged particles, it can be assumed quasisteady and can be updated periodically. Thus, the PIC-MCC code provides the ionization information, including electron energies and density distribution, for the neutral calculation, and the view factor model is used to update the background neutrals for the particle simulation. Finally, the combined simulation would converge when all the distributions of neutrals, ions, and electrons remain stable. The coupling model is described in detail as follows.

Firstly, the EP chamber is divided into surfaces so that the view factors and ionization parameters can be calculated. As shown in Fig. 5, the inner EP chamber wall is

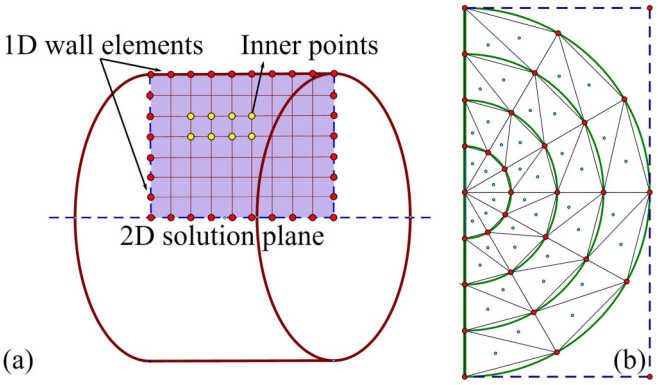

FIG. 5. (a) Inner chamber walls are divided by the 1D elements. (b) 2D triangles are used to approximately extend all the 1D wall elements.

first divided into 1D elements, each of which represents a ring of the chamber wall. Note that all the divisions are not made on the outer walls, because the outer neutral flux is not considered in this model. Then the two-dimensional (2D) solution plane is selected to do the simulation and calculate the physical parameters. Inner nodes (yellow points in the figure) are generated on the plane. Two-dimensional triangles are used to approximately extend all the 1D wall elements and the green points are the geometric center of each triangle.

Secondly, a matrix representing the interrelationship of the wall elements to determine the neutral flow balance is established.

By continuity, the summation of the thermal view factors of an element is 1. For a given wall elements h (the inner wall elements), the thermal view factors are normalized using an identical factor to satisfy the neutral-flux continuity as given by Eq. (12).

$$\sum_m \Psi_{hm} = \sum_m \sum_{t_m} \Psi_{ht_m} \equiv 1, \tag{12}$$

where t_m refers to the triangle elements of 1D element m.

With all the view factors between wall elements defined, an expression for the neutral flow continuity between the wall elements is determined. For steady-state continuity, the neutral flow (Y) of a given wall element (h) must equal the sum flow from all other wall elements (m), gas sources (s), and the local wall recombination (r), as given by Eq. (13).

$$Y_h = \sum_m V_{mh} Y_m (1 - \zeta_{o,m}) + \sum_s V_{sh} Y_s + Y_{rh}, \tag{13}$$

where $\zeta_{0,m}$ is the transparency of wall element m.

Y_h, Y_m, Y_s represent the neutral flow from wall element h, m and the real gas source s, respectively. Y_{rh} is the recombination part which occurs on wall elements h. Equation (13) is suitable for all wall elements so we can determine the neutral flux of the whole inner surface of the EP discharge chamber by an invertible matrix [Eq. (14)].

$$\begin{bmatrix} 1 & [-V_{21}(1-\zeta_{o,2})] & \cdot & \cdot \\ [-V_{12}(1-\zeta_{o,1})] & 1 & [-V_{32}(1-\zeta_{o,3})] & \cdot \\ \cdot & \cdot & \cdot & \cdot \\ \cdot & \cdot & \cdot & \cdot \end{bmatrix} \begin{bmatrix} Y_1 \\ Y_2 \\ Y_3 \\ Y_4 \end{bmatrix} = \begin{bmatrix} \sum_s V_{s1} Y_s + Y_{r1} \\ \cdot \\ \cdot \\ \cdot \end{bmatrix}. \tag{14}$$

Thirdly, all neutral view factors V would be calculated to make the information of the matrix complete.

For the neutral view factor (V), β must be calculated. According to Eq. (12), the electron ionization rates K_{iz}^s, K_{iz}^p [in Eq. (9)] need to be determined first, which can be calculated as

$$K = \int_0^\infty w f(w) \sigma(w) dw, \tag{15}$$

where w is the velocity of particles, $f(w)$ is the distribution function of w, and $\sigma(w)$ is the collision cross section. K is calculated in a statistic form [45] as in Eq. (16) and averaged every 5000 steps as in Eq. (17), where all the parameters can be obtained from the PIC-MCC code.

$$K = \sigma\left(\frac{1}{2} m \langle w \rangle^2\right) \langle w \rangle, \tag{16}$$

$$K = \sum_{i=1}^{5000} \sigma_i w_i / 5000. \tag{17}$$

As we assume a constant velocity of neutrals, β can be calculated as

$$\beta = \sum_n \left[\left(K_{iz}^s n_s + K_{iz}^p n_p \right) dt \right]_n, \tag{18}$$

where in Eq. (18), the neutral integral path is divided into n equal divisions, so that the calculation time for each division is dt. The PIC-MCC method is used to obtain the electron density (n_s, n_p) from each grid, and to calculate the electron velocity w, and the electron-neutral collision cross section $\sigma(w)$, in Eq. (16).

As shown in Fig. 6, the integral path is divided into several points (yellow points on the path), which are projected on the 2D solution plane referred to in Fig. 5 using a solid ring method. The positions of the points on the path are transferred into the Z-R plane as given by Eq. (19). As the integral path

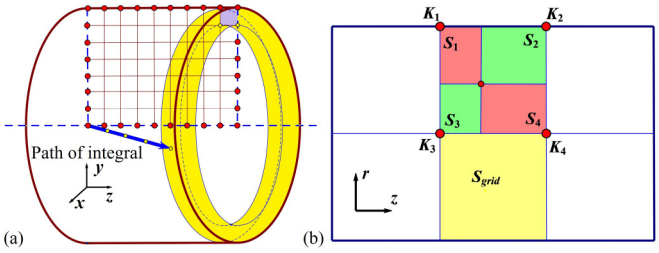

FIG. 6. (a) The division methods of the integral path. (b) The area weighting method for calculating K.

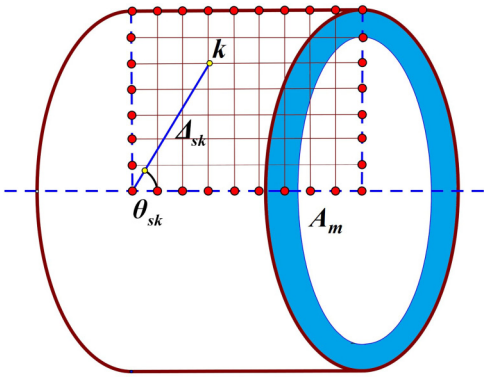

FIG. 7. The illustration of the variables used in Eqs. (21)–(23).

is divided into n equal divisions, for the parameter K, we use the area weighting method to the get the values at the in-cell dispersed points from surrounding grid nodes, as given by Eq. (20).

$$z = z, \qquad r = \sqrt{x^2 + y^2}, \tag{19}$$

$$K = \frac{K_1 S_4 + K_2 S_3 + K_3 S_2 + K_4 S_1}{S_{\text{grid}}}. \tag{20}$$

Depending on whether there is any block between two specific differential surfaces, the geometry factor G is set to 0 (blocked) or 1 (unblocked). Thus, all the values of $V_{mh} = G_{mh}\beta_{mh}\Psi_{mh}$ are calculated, and the neutral densities on each grid can be determined.

y_m is defined as the unitary neutral flow on wall elements m, and y_{sk} is the flow from the real gas source to the inner node k, as given by Eqs. (21)–(23).

$$y_m = Y_m / A_m, \tag{21}$$

$$y_{sk} = Y_s \beta_{sk} \Theta_{sk}, \tag{22}$$

$$\Theta_{sk} = \frac{\cos(\theta_{sk})}{\pi \Delta_{sk}^2}. \tag{23}$$

The variables used in Eqs. (21)–(23) are shown in Fig. 7. Δ_{sk} refers to the distance between the real gas source and the inner node k. θ_{sk} is the angle between the central axis of the chamber and the straight line between the real gas source and the inner node k. The filled blue part represents the area A_m of element m.

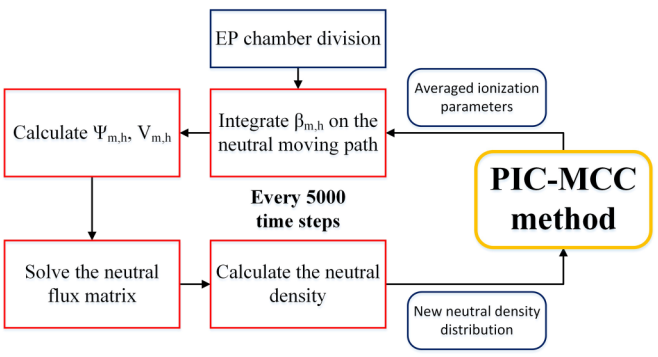

FIG. 8. The entire scheme combining the view factor model with the PIC-MCC method.

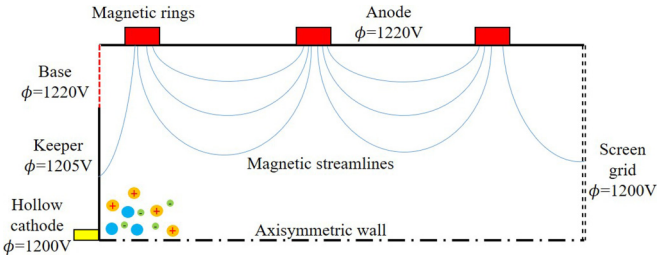

FIG. 9. The potential settings on the different boundaries.

The densities from the wall and the real gas source both contribute to the density of an inner node k as given by Eq. (24). $\bar{C}$ refers to the mean speed of the neutrals from the wall or the real gas source, which is determined by the local temperature as given by Eq. (25).

$$n_k = 4 \sum_m V_{mk}(1 - \zeta_{o,m}) \left(\frac{y_m}{\bar{C}_m} \right) + 4 \sum_s \frac{y_{sk}}{\bar{C}_s}, \tag{24}$$

$$\bar{C} = \sqrt{\frac{8kT}{\pi m}}. \tag{25}$$

To determine the density at a wall element h, we use both the incident and outgoing fluxes for the unit hemisphere surrounding the element. The resulting expression for the neutral density of a wall element (n_h) can be determined as given by Eq. (26).

$$n_h = 2\frac{y_h}{\bar{C}_h} + 2 \sum_m V_{mh}(1 - \zeta_{o,m}) \frac{y_m}{\bar{C}_m} + 2 \sum_s \frac{y_{sh}^w}{\bar{C}_s}, \tag{26}$$

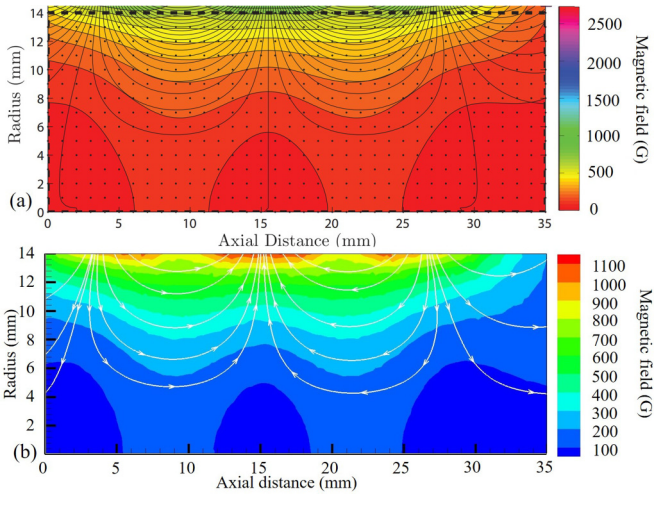

FIG. 10. (a) UCLA experimental data and (b) simulated magnetic flux density. Note that the color scales are not the same for simulation and experimental results.

TABLE II. Treatments for different particles on the boundaries.

	Neutrals	Electrons	Ions
Hollow cathode	Diffuse reflection	Absorbed	Absorbed
Base	Diffuse reflection	Mirror reflection	Mirror reflection
Anode	Diffuse reflection	Absorbed	Absorbed
Screen grid	Diffuse reflection or passing through	Mirror reflection	Absorbed or passing through
Axis	Mirror reflection	Mirror reflection	Mirror reflection

where y_{sh}^{w} is determined as given by Eq. (27).

$$y_{sh}^{w} = Y_s \beta_{sh} \Theta_{sh} = Y_s \left(\frac{\sum_{t_h} \beta_{st_h} \Theta_{st_h} A_{t_h}}{\sum_{t_h} A_{t_h}} \right). \tag{27}$$

The entire process of the view factor model algorithm combined with the PIC-MCC method is explained in Fig. 8. Updates of the neutral distribution using the view factor model are applied every 5000 time steps of the PIC-MCC calculation. Before calculating the neutrals, the EP chamber is divided into 1D elements and then into 2D triangles. The averaged ionization parameters, which determine the parameter K, are from the PIC-MCC method. Thus, the neutral ionization fraction for elements m and h (β_{mh}), can be integrated on the neutral moving path by parameter K and electron densities (n_s and n_p). Then Ψ_{mh}, V_{mh} and the neutral flux matrix can be calculated and established. By solving the matrix, the neutral flux for each element is determined. The new neutral distribution is calculated from the flux data and is used as input for the next-step PIC-MCC iteration. Only when the ions, electrons, and neutrals all come to convergence will the iterations of this algorithm be terminated.

III. SIMULATION

This simulation is based on the UCLA miniature ring-cusp discharge experiment [34,35]. The discharge chamber has a diameter of 28 mm and a length of 35 mm, and the propellant feed is xenon in 0.5 SCCM (cubic centimeter per minute at STP).

We assume the real gas source as a point source located on the axis and divide the geometry simulation region into 175×70 grids on the axial and radial direction, respectively. The time step of electrons is set as 1×10^{-11} s. The macroparticle method is used to represent a vast number of particles in a macroparticle. One neutral macroparticle represents 10^7 actual neutrals, while it is 10^5 in the case of electrons and ions.

To shorten the computational time without parallel methods, different numerical acceleration methods have been used in our PIC-MCC simulation. Reducing the heavy particle mass can lessen the computational burden. The mass of heavy particles has been reduced by a factor f ($f = m_{\text{artificial}}/m_{\text{real}} < 1$) compared with the real mass so that the ions can move much faster due to the same electromagnetic force but a smaller mass. The faster ions result in a reduction in the ion convergence time, and further accelerate the entire simulation [3]. The modifications and applications of this method have also been described in Refs. [3,27].

Artificial permittivity is used to reduce the time step and to enlarge the mesh size. The time step in the PIC-MCC method is determined by the shortest time of all the characteristic times in the physical progress, which is usually the electron oscillation time [Eq. (28)]. The mesh size is determined by the Debye length [Eq. (29)].

$$\omega_{pe} = \sqrt{\frac{e^2 n_e}{\gamma^2 \varepsilon_0 m_e}}, \quad \Delta t \leqslant \frac{0.1}{\omega_{pe}}, \tag{28}$$

$$\lambda_d = \sqrt{\frac{\gamma^2 \varepsilon_0 K_b T_e}{e^2 n_e}}, \quad \Delta x \leqslant \frac{\lambda_d}{0.3}, \tag{29}$$

where n_e is the number density of electrons, m_e is the electron mass, T_e is the electron temperature, and e is the electron

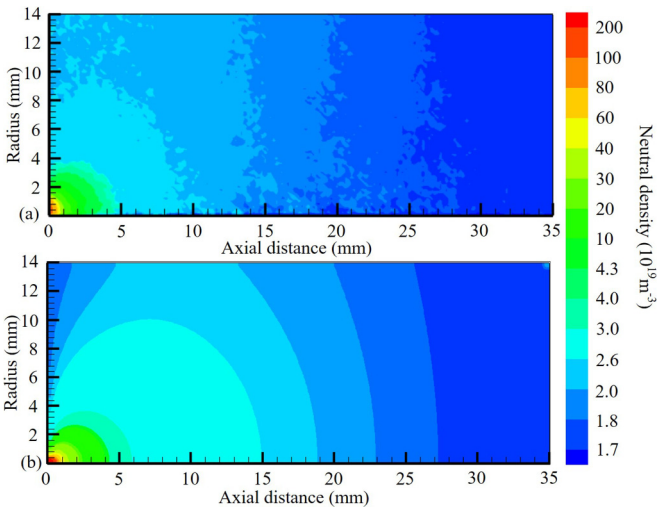

FIG. 11. The neutral distribution simulated using the full PIC-MCC code without the numerical acceleration methods (a), and using the view factor model (b).

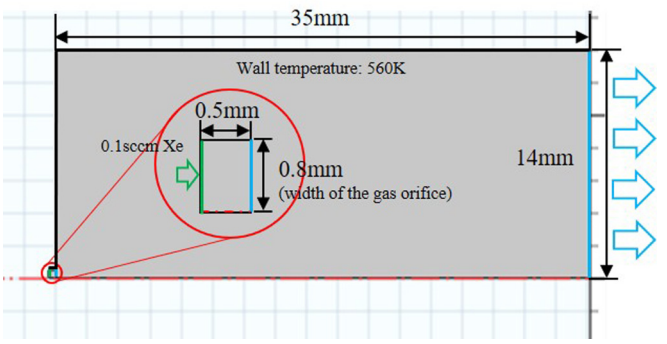

FIG. 12. The settings in the COMSOL free molecules simulation.

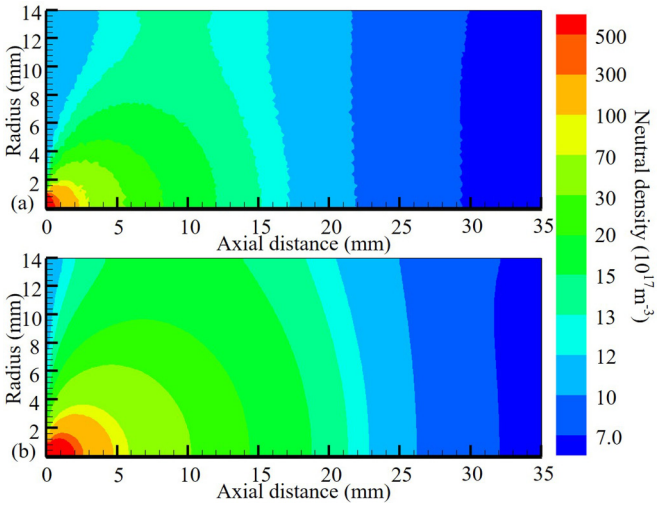

FIG. 13. The simulation results for the neutral density using COMSOL (a), and the view factor model (b).

charge. γ^2 is defined as the ratio of the artificial vacuum permittivity to the real one, ε_0. By adopting $\gamma^2 > 1$ ($\gamma^2 = \varepsilon_{\text{artificial}}/\varepsilon_0$), an artificially enlarged vacuum permittivity leads to larger time steps and mesh sizes [3], both of which can reduce the computational scale by simulating fewer steps and meshes.

A scaling method [36] is added in the simulation code which is used by many researchers [12,19], to reduce the simulation domain by $1/\xi$ times. This method is a self-similarity method, keeping dimensionless numbers of plasma unchanged to guarantee the main physical progress real. ξ is the scaling factor representing the ratio of simulation length to the real length.

Moderate numerical acceleration parameters, where $\gamma^2 = 5^2$, $f = 0.5$, $\xi = 0.1$, have been used in this manuscript, which cause relatively lower plasma density and slightly thicker sheaths. Nevertheless, we set strict restrictions to ensure that the two groups of results are simulated in exactly the same conditions except for the treatment of the neutrals.

Three identical magnetic rings are placed around the discharge chamber, with equal axial spacing between each one. Samarium cobalt (Sm_2Co_{17}) is used for three magnetic rings, with a permeability of 1.36 and a remanence of 1.05 T. The boundary conditions are separated into six parts, as shown in Fig. 9 to match the experiment.

As the current generated by the plasma is relatively small, the self-aligned field is neglected in this paper. The magnetic field is precalculated and set as a constant input for the simulations herein. The profiles of the magnetic field in the simulation and the experiment are compared in Fig. 10.

Electrons are emitted from the hollow cathode to the discharge chamber and heated by the emitter plasma. Therefore, the heated electrons are accelerated by hollow cathode discharge voltage. The electron discharge current is set to 0.38 A and the electron temperature to 5 eV.

When particles move to the boundaries, different treatments are used in the simulation model, shown in Table II. Chamber walls can emit low-energy secondary electrons when impacted by the ions. The probability of this depends on the wall material and ionization energy, which is specified using the measured secondary electron emission coefficients. In this model, the secondary electrons emission coefficient for single charged ions and double charged ions is taken as 0.058 and 0.4 [16]. Furthermore, transparency is used to account for the probabilities whether the particles can pass through the boundary or not.

For coupling the neutral view factor model with the PIC-MCC code, we list several assumptions, conditions, or simplifications below.

(1) For the micro-ion thrusters investigated herein, the average Knudsen number for neutral collisions (including neutral-neutral and charge-exchange) is greater than 1.0 [33,46], so the model can be simplified as a noncollision one.

(2) When the recombination is ignored due to its small account, the essential continuity equation matrix can be simplified as given by Eq. (30).

$$\begin{bmatrix} 1 & [-V_{21}(1-\zeta_{o,2})] & \cdot & \cdot \\ [-V_{12}(1-\zeta_{o,1})] & 1 & [-V_{32}(1-\zeta_{o,3})] & \cdot \\ \cdot & \cdot & \cdot & \cdot \\ \cdot & \cdot & \cdot & \cdot \end{bmatrix} \begin{bmatrix} Y_1 \\ Y_2 \\ Y_3 \\ Y_4 \end{bmatrix} = \begin{bmatrix} \sum_s V_{s1} Y_s \\ \cdot \\ \cdot \end{bmatrix}. \tag{30}$$

(3) The neutrals are at constant velocity (300 m/s) due to the setting of uniform wall temperature at 560 K. As the experimental data are set as ~500 K [34] and vary in the range of 450–525 K [35], the uniform-temperature assumption is reasonable when the differences in the temperature distribution are small.

(4) The transparency value of the screen grid is 0.1, while for other surfaces, it is 1.

(5) No shadings exist between all surfaces so $G \equiv 1$, $V = \beta V$.

We use the view factor model to update the neutral distributions every 5000 PIC time steps. This simulation case has been set as the experimental group. Meanwhile, we set a fixed-neutral model as a control group, where the simulation conditions are the same as in the view factor model except the neutrals are fixed as a constant background distribution. For the fixed-neutral model, as the neutrals are actually consumed due to the ionization during the discharge progress, the fixed background distribution is calculated assuming for 40% of real gas flow (0.2 SCCM) from the cathode [17]. To get the most accurate result, the background distribution is simulated by the full PIC-MCC code, which treats neutrals as particles and uses no numerical acceleration methods.

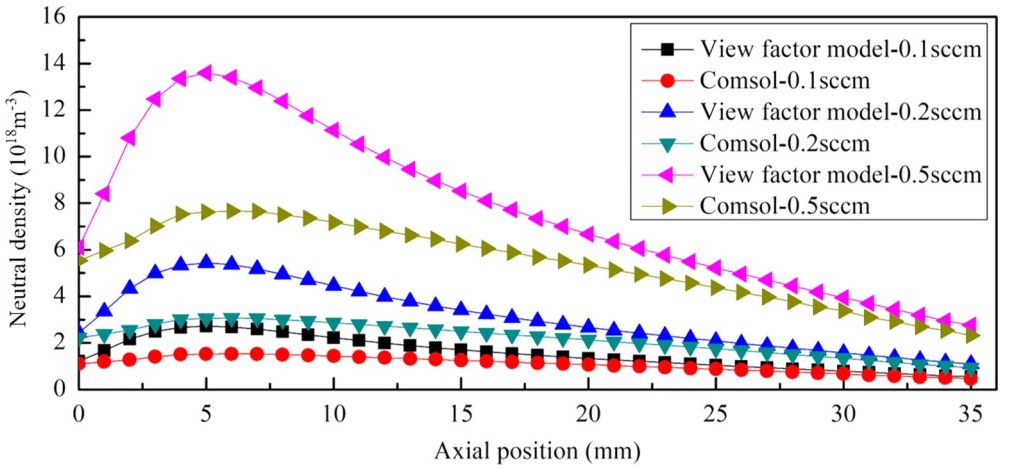

FIG. 14. The neutral density change along the axial position (at $r = 7$ mm) for different gas flow rates.

IV. RESULTS AND DISCUSSIONS

A. Verification of the view factor model

We compare simulations using the view factor model with the nonaccelerated full PIC-MCC code for a case with 40% gas flow (0.2 SCCM) with discharging effects neglected. The resulting distributions are shown in Fig. 11. The main features and magnitude of the spatial distribution for the simulations using the view factor model match well with the nonaccelerated full PIC-MCC code. The main errors appear near the point gas source, caused by the 2D simplification. As our model is a two-dimensional and axisymmetric one, we use y_m and y_{sk} to simplify the neutral flux from the elements and points to the elements. y_{sk} in Eq. (22) is determined based on the view factor from the point gas source to the interior points. However, in this simplification, the item Θ_{sk} [Eqs. (22) and (23)] in y_{sk} is only valid when two points are far enough apart. So, the simulation errors in the neutral distribution occur near the gas source because the interior points and the point gas source are close to each other.

The simulation wall-clock time for our model is 345 s, while the conventional full PIC requires over 48 h. Compared with the full PIC method, this method takes only 0.2% of the time for the same distribution calculation. These results illustrate that the view factor is a fast and relatively accurate way to simulate the neutral distribution.

Neutral distribution simulations have also been carried out using COMSOL to compare with the results of the one using the view factor model. We set the same domain shape and properties as the miniature ring-cusp discharge experiment, except for a 100% transparency for the neutrals on the right side of the chamber. The free molecular flow module, one of COMSOL's components, is used to evaluate the accuracy of the nonionized neutral distribution simulated with the view factor model.

The free molecular flow module of COMSOL MULTIPHYSICS (COMSOL, Inc.) has also been applied in Refs. [47,48], which use the angular coefficient method [49] for the molecular simulations. The settings of the COMSOL simulation are shown in Fig. 12. The 2D axisymmetric model is used in the simulation, where the red dashed line denotes the axis. Different boundary conditions are set in this simulation. The green boundary is the entrance of the propellant (0.1 SCCM Xe in this case). The black boundaries are the thruster walls, for which temperature is uniform at 560 K, the same as the view factor model. The blue boundaries are the ones that Xe gas flow can pass freely. Unstructured meshes ranging from 0.002 66 to 0.5 mm are used in this case. COMSOL creates this virtual 3D geometry by revolving the 2D surface mesh into a 3D mesh. For each

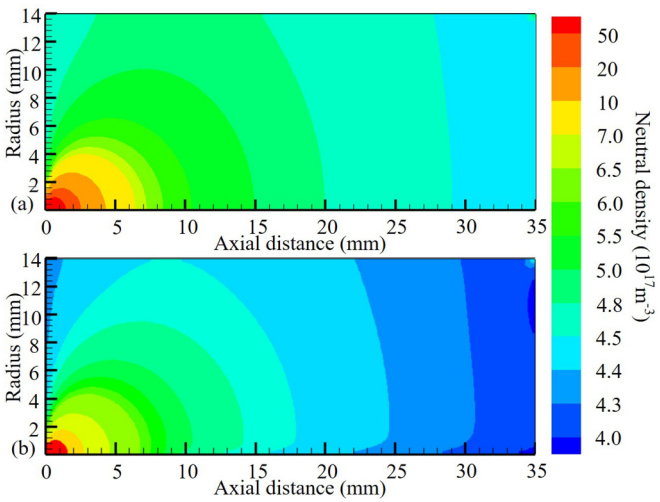

FIG. 15. (a) The initial distribution of neutrals. (b) The distribution of neutrals in the final steady state.

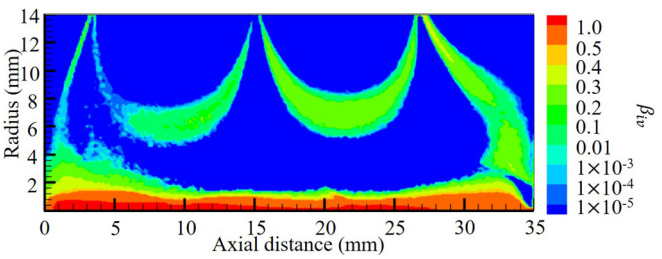

FIG. 16. The distribution of β_{iv}, which represents the ionization capacity at different locations.

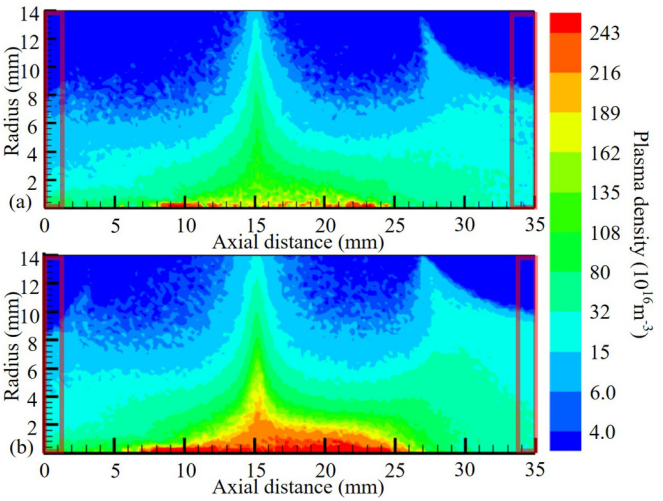

FIG. 17. The plasma density from the fixed-neutral model (a), and the view factor model (b). (Note that the color scales are not the same as the experimental data.)

mesh i, the arriving flux per unit area, G_i, and the total number density, n_i, are determined by Eqs. (31) and (32).

$$G_i = -\int_{S'} \frac{J_{i'}(\mathbf{n}\cdot\mathbf{r})(\mathbf{n}'\cdot\mathbf{r})}{\pi r^4} dS', \tag{31}$$

$$n_i = -\int_{S'} \frac{J'_i(\mathbf{n}\cdot\mathbf{r})(\mathbf{n}'\cdot\mathbf{r})}{\pi r^3}\left\langle\frac{1}{c'_{3D}}\right\rangle dS' + 2\left\langle\frac{1}{c_{3D}}\right\rangle J_i,$$

$$\left\langle\frac{1}{c'_{3D}}\right\rangle = \sqrt{\frac{\pi M_n^i}{8RT'}}, \tag{32}$$

where for each mesh i, J'_i is the incident flux, J_i is the outgoing flux, M_n^i is the mass of different particles (only ^{131}Xe in this case). $\mathbf{n}$ and $\mathbf{n}'$ are the normal vectors of surface S and S'.

The neutral densities (at 0.1 SCCM) are compared in Fig. 13, which demonstrates that the view factor model can simulate the neutral accurately in both trend and magnitude. The density trends remain the same for different orifice width settings, indicating a high density near the orifice and decay along the Z direction. However, the density distributions

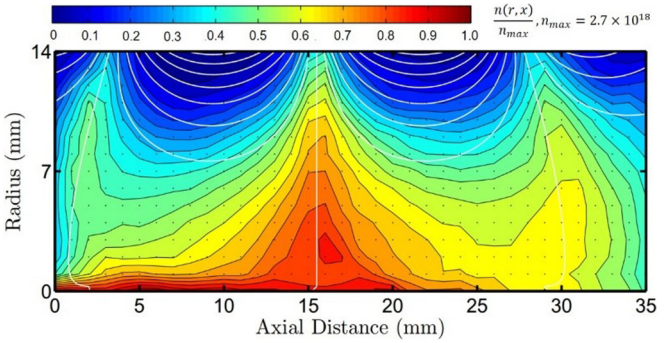

FIG. 18. The plasma density from the UCLA experimental data, which are normalized by the maximum plasma density value.

change dramatically for the smallest orifice widths for which the traversal of the gas is more restricted.

The density changes at $r = 7$ mm are shown in Fig. 14. The trends in the changes match well between the two approaches, for which the density tends to first increase near the gas source and then decrease along the axial position. As the relatively low-density area dominates the discharge chamber, the differences between both approaches are small so the global accuracy is guaranteed. Higher density appears near the gas orifice region, and only in a small portion of the chamber.

The differences between the COMSOL and the view factor models are caused by the gas orifice settings. In the view factor model, the gas source is set as a point source which has no width at all so that the flux can traverse in all directions with a Maxwellian-Boltzmann distribution in each velocity component. Meanwhile, the gas source setting in COMSOL is to set a small-width orifice which the gas can pass through and then traverse to all of the chamber volume. Thus, unlike for the case of the point source, the gas molecules first flow in almost the same directions and then change to different ones to fill the chamber. Different distributions of neutrals occur due to the different gas orifice sizes.

B. Parameters of the thrusters

Here, using the UCLA experimental data, simulations of the entire discharge chamber of the UCLA miniature ring-cusp discharge experiment are discussed and compared.

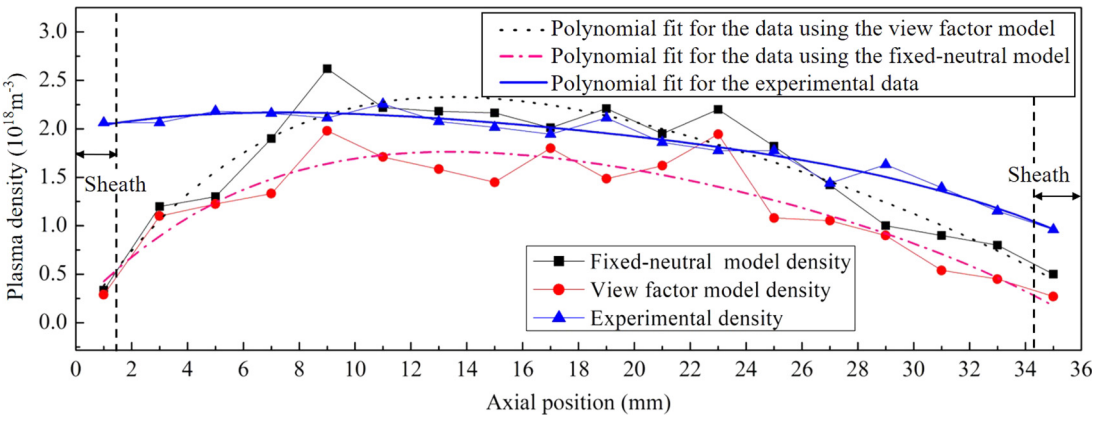

FIG. 19. The polynomial fit for the neutral density along the axis (at $r = 0$ mm).

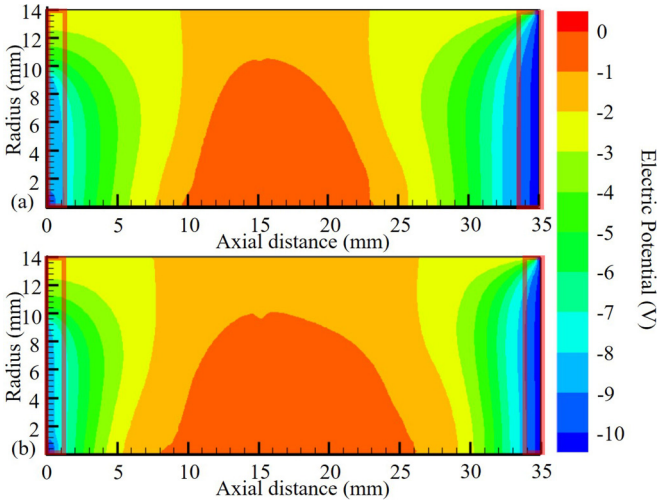

FIG. 20. The electric potential in simulation results for the fixed-neutral model (a), and the view factor model (b).

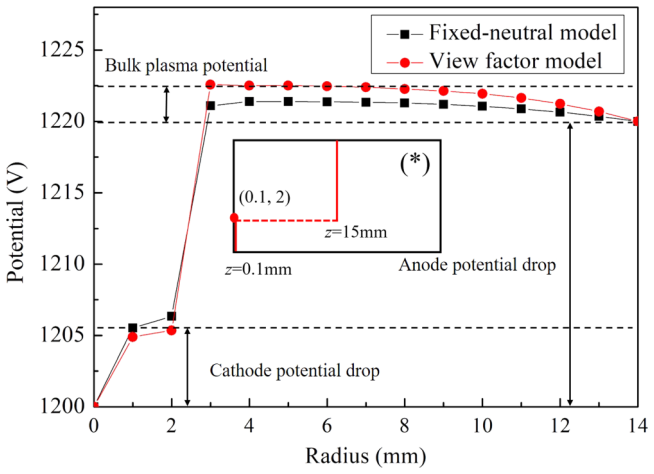

FIG. 21. Radial potential profiles in the discharge chamber using both simulation methods. The inset shows the notation of the plotting track.

The initial neutral distribution and the converged one are discussed first. As shown in Fig. 15, the neutrals have significantly decreased from the initial to the stable case, but not as much as assumed for the fixed-neutral model. The density distribution changes in shape and mainly decreases at the axis, due to the ionization rate differences for the neutrals in the chamber.

An intermediate variable to calculate β, β_{iv}, is defined in Eq. (33) to account for the neutral consumption differences.

$$\beta_{iv} = K_{iz}^{s} n_s + K_{iz}^{p} n_p. \tag{33}$$

β_{iv} represents the velocity and density information of electrons in the discharge chamber. Large β_{iv} appears at the position where a large number of electrons or fast electrons exist, causing easier ionization for neutrals passing through. As Eq. (18), $\beta = \sum_n [\beta_{iv} dt]_n$, Fig. 16 illustrates the spatial dependence of β_{iv} distribution. The value of β_{iv} is much larger at the position of the real gas source and along the axis. Due to the magnetic rings, small β_{iv} appears along the magnetic lines. However, in most regions where magnetic field has little influence, β_{iv} equals 0.

Although β_{iv} along the magnetic lines is not 0, it is too small to have a significant integral effect. Ionization of neutrals is only significant along the axis because of the large and dense β_{iv} along the axis. This kind of stratified neutral distribution has also been found in the research of NSTAR [50].

We now compare the simulation results using the fixed-neutral [Fig. 17(a)] and the view factor models [Fig. 17(b)] against the experimental results for the plasma density in the thruster (Fig. 18). The red parts are the sheaths region, where the numerical acceleration method of the PIC-MCC can cause a lower plasma density.

Although the trend of the distributions is the same, the global density using the view factor model is higher than the one using the fixed-neutral model. In the discharge area, located near the axial position $x = 15$ mm, the density distribution matches the experimental one better when the view factor model is used. This illustrates that the change of the density distribution of neutrals can significantly influence the discharge process, leading to more ions and denser plasma in the discharge chamber.

The simulation data and polynomial fits for the neutral density along the axis (at $r = 0$ mm) are shown in Fig. 19. The solid blue line represents the experimental data, while the solid red line (with circles) and the black one (with squares) represent the simulation results for the fixed-neutral model and the view factor model, respectively. The experimental distribution data show the highest and the most uniform plasma density. The simulation results using the view factor model and the fixed-neutral model show close to the experimental data in the discharge area, but a dramatically low density in the sheaths. This happens because the numerical acceleration methods of the PIC-MCC code can influence the physical parameters in the sheaths depending on the magnitudes of γ^2 and f [16]. The sensitivity of using these numerical acceleration methods is analyzed in Ref. [27].

The density profile using the view factor model in the discharge area fits better than the one using the fixed-neutral model as the changing neutrals make the plasma distribution more realistic. Especially for the bulk plasma area, the simulation results using the view factor model fits the ex-

TABLE III. Comparison of macroscopic parameters from the simulations and experimental data.

	Discharge current (mA)	Current simulation error (mA)	Discharge power (W)	Power simulation error (W)
Experimental data	500	–	10	–
Fixed-neutral model	400.9	99.1	8.018	1.982
View factor model	450.8	49.2	9.016	0.984

TABLE IV. Main simulation environment settings for the two computers.

Central processing unit (CPU)	Memory	Integrated development environment (IDE)	Operating system
Intel i7-8700	8 GB × 4 = 32 GB	MICROSOFT VISUAL STUDIO 2015	WIN 10 (1709 version)

perimental data quite well. Along the axis the view factor model gives an averaged density of $1.65 \times 10^{18}\ \mathrm{m}^{-3}$ while the fixed model gives $1.22 \times 10^{18}\ \mathrm{m}^{-3}$ and the value of averaged experimental data is $1.87 \times 10^{18}\ \mathrm{m}^{-3}$. Compared with the fixed-neutral model, the simulation error for the view factor model decreases from 35% to 12%, agreeing better with the experimental data.

As we mentioned before, the profile of the magnetic field is an input for the simulations, which is as for the UCLA device. The other parameters and profiles for the simulations also correspond to the UCLA device. However, the simulation results for the potential distribution (Fig. 20) do not match well with the experimental data [35]. The highest potential appears in the bulk plasma area in the simulation but near the anode wall in the experiment.

The radial potential profiles from both simulations are plotted in Fig. 21 and the radial plotting track is shown in the inset of Fig. 21. As the cathode is located at the point gas source, we plot the radial potential of the first 2 mm close to the left wall (along $z = 0.1$ mm) and the remaining 12 mm along $z = 15$ mm. This figure shows that the data match well with typical ion thrusters [50,51]. In these, the potential is highest in the bulk plasma area and drops in the sheath regions. On the other hand, the experimental data are different from our simulation in that the potential is highest near the anode wall. As the author associated with the UCLA device explained, the experimental data showed a nontypical ion thruster, in which the potential structure is indicative of an overconfined plasma. The strong magnetic field in the device may overconfine the electrons near the anode wall, resulting in a slightly lower plasma potential in the bulk plasma area [35].

Furthermore, our simulation results match most ion thruster simulations using PIC methods [18,51,52]. Also, the nontypical distribution usually only appears in devices with a very strong magnetic condition (e.g., with additional coils) [53,54]. In our opinion, the disagreement is caused by the view factor model, but may be caused by the simulation errors in the presheath and sheath regions. Acceleration methods could influence these regions so some physical phenomenon (i.e., the overconfined electrons near the anode wall) could be missed there. Nevertheless, the quantitative difference in the potential between the simulation results and the experimental data is small. As the simulation results in the bulk plasma area are still valid, the process of main discharge is not affected, and the results for the other parameters from the simulations are expected to agree well with the experimental data.

For the two simulation cases herein, the electric potential distributions using the view factor model and the fixed-neutral model show few differences and very similar evolution. Both simulation distributions show obvious potential drops near the left and right walls (the red parts), which correspond to the lower plasma density in the red parts of Fig. 17. In Figs. 17 and 21, both of the red parts are the thicker sheath regions in the simulations, which are caused by the acceleration methods. In the sheath regions, the plasma density is much lower than that in the bulk plasma (shown in Fig. 19) and obvious potential drops appear.

The comparisons of macroscopic parameters are shown in Table III. Equation (34) shows the relationship between the discharge power and the discharge current. The simulation error in discharge current and power decreases from 19.8% to 9.8%. Thus for these macroscopic parameters, the simulations using the view factor model agree better with the experiments.

$$P_d = I_d(V_{\mathrm{anode}} - V_{\mathrm{cathode}}). \tag{34}$$

C. Convergence and simulation time

We use two personal computers to conduct the simulation and set strict restrictions for the two models to ensure that the simulation environment is exactly the same. The main parameters are shown in Table IV.

For the fixed-neutral model, only ions and electrons should be taken into account when discussing the convergence, as shown in Fig. 22(a). The fixed-neutral model takes about 1 800 000 time steps to converge.

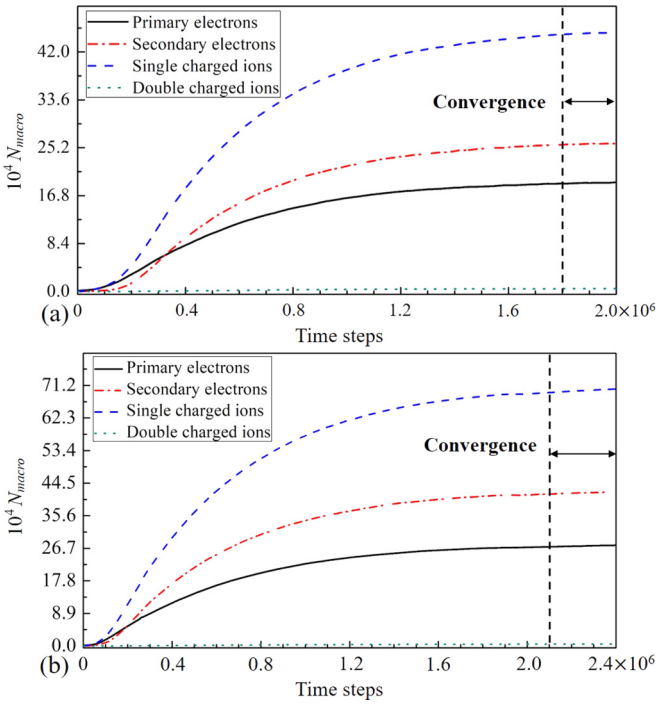

FIG. 22. (a) The macroparticle numbers (N_{macro}) curve of the fixed-neutral model (a), and view factor model (b). It should be noticed that the number of macroparticles for double charge ions are few but nonzero, about 5175 in (a) and 5033 in (b).

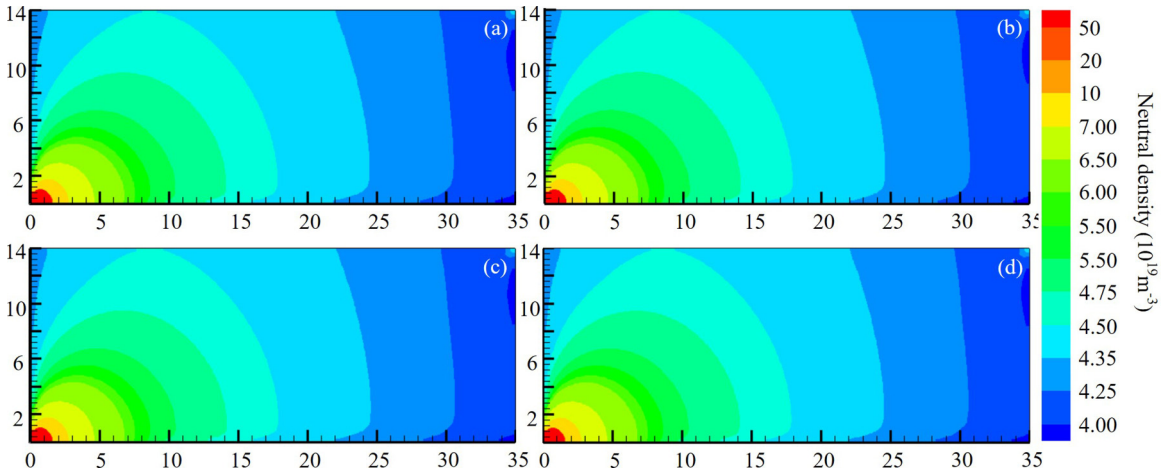

FIG. 23. The neutral distributions from 2 050 000 to 2 200 000 time steps using the view factor model: (a) 2 050 000 time steps; (b) 2 100 000 time steps; (c) 2 150 000 time steps; (d) 2 200 000 time steps.

To determine the convergence, the PIC-MCC code with the view factor model should take into account not only ions and electrons but also the neutral density, as the neutrals are the slowest to converge. The particle number curves (neutrals not included) are shown in Fig. 22(b) and the neutral density evolution is shown in Fig. 23. The neutral distributions show almost no change from 2 050 000 to 2 200 000 time steps, while there are 2 100 000 when the ions and electrons are convergent. Hence, regarding the slowest neutrals, the entire simulation using the view factor model reaches convergence.

Because of the greater computational demand, the view factor model uses a longer time (599 h) to converge than the fixed-neutral model (452 h), that is, 32.5% longer for the view factor model to simulate exactly the same case. The analysis of the time advance can help us know which part of computation matters the most and make optimizations in other simulation cases.

The view factor model mainly influences the simulation time in three ways. First, because of more accurate and denser plasma, the update of the particle number requires more computational time. In this case, particles increase enormously as shown in Table V, which dominates the time advance.

Secondly, the time steps required by the two models are different as well. The simulation case takes 300 000 (16.7%) more steps by using the view factor model compared to the one using the fixed-neutral model. For simplification, we assume that the time steps are calculated equally long in the time-advance analysis. However, for the view factor model, more particles are calculated in one time step, leading to nonequal calculation time and extra time increase. Nevertheless, we can still classify this portion of time advance as the influence of the particle advance.

Finally, the computational cost of the view factor model itself makes a difference as well. It costs about 350 s to iterate a new neutral distribution each 5000 time steps. This part of the calculation takes 420 iterations to converge in 2 100 000 steps, using a total of 40.8 h.

The influences of the different calculation parts are listed in Table VI, which gives an approximate sense of the time advance when using the view factor.

For the same case using the same computational environment, the full-PIC code has been applied but still did not converge after 3 months. The simulation time comparison is shown in Table VII; the view factor saves more than 72.3% of the time to reach a convergence compared with the full-PIC method. From all the analyses above, the application of the view factor model on the PIC-MCC code is a good compromise between the computational time and the accuracy of the simulation.

V. CONCLUSION

A PIC-MCC method has been designed that employs the view factor model to iterate neutrals periodically, thereby improving the accuracy of the simulation. The algorithms to combine the view factor model and the typical PIC-MCC code are presented in this paper. We verify the neutral distribution in a nondischarge case and simulate the UCLA miniature ring-cusp discharge device. The UCLA experimental device with a gas flow rate of 0.5 SCCM and a discharge current of 0.5 A, is simulated using the PIC-MCC code with the fixed-neutral model and the view factor model, respectively. Compared with the fixed-neutral model, the view factor model updates the neutral distribution each 5000 PIC time steps.

TABLE V. Comparisons on the macroparticle numbers between the view factor model and fixed-neutral model.

Macroparticle numbers when converged	View factor model	Fixed-neutral model	Increase percentage (%)
Primary electrons	277000	192300	44.0
Secondary electrons	421800	260600	61.9
Single charged ions	704200	456400	54.3
Double charged ions	5175	5033	2.8

TABLE VI. Extra simulation time of view factor model for different calculation parts.

Total time increase (h)	View factor model cost (h)	Time step advance (h)	Particle advance (h)
147(100%)	40.8(27.8%)	24.5(16.7%)	81.6(55.5%)

TABLE VII. Simulation time for different models for the same simulation case. The fixed-neutral model is set as the time base.

Fixed-neutral model (h)	View factor model (h)	Full-PIC (PIC-MCC method) (h)
452(100%)	599(132.5%)	>2160 (>477.9%)

The simulation results using the view factor model agree better with the UCLA experimental results for the distribution of plasma density, neutral density, and electric potential in the discharge chamber. The simulation errors in the average plasma density along the axis decrease from 35% to 12%. For the macroscopic parameters, the simulation errors in the discharge current and discharge power decrease from 19.8% to 9.8%.

Convergence time analysis has been carried out for the same cases under the same simulation environment. The simulation using the fixed-neutral model reaches convergence in a shorter time compared with the view factor model, while the full-PIC method (treating neutrals as particles) still did not converge after 2160 h. The time costs for these three methods are 100:133:(>478), illustrating that the view factor model notably reduces the computational time compared with the full-PIC method. Meanwhile, the simulation time for the view factor method only increases by 33% compared with the fixed-neutral model. The extra simulation time for the view factor model mainly consists of three parts: the extra iteration of the view factor method (28%), the time step advance (17%), and the particle advance (55%), which suggests that the particle advance dominates the extra computational cost.

This application of the view factor model provides an alternative way to simulate the neutral distribution in the particle simulation of plasma, achieving a balance between accuracy and speed. However, some of the simplifications should be modified in future work. A nonuniform temperature distribution should be taken into consideration to make the neutral velocity distribution more reliable. Furthermore, the PIC-MCC code can be parallelized to accelerate the simulation speed and a 3D model will also be developed to make the neutral distributions more accurate. In the future, this model can be used in the PIC simulations of Hall-effect thrusters, MPD thrusters, and other plasma-related devices, to shorten the simulation time and investigate the internal physical mechanisms.

ACKNOWLEDGMENTS

This work is supported by the National Natural Science Foundation of China (Grant No. 11872093). The authors give special thanks to Dr. Baojun Wang and Dr. Guangchuan Zhang, who provided much professional help. Special thanks are also given to Dr. Samuel J. Araki, in the Air Force Research Laboratory, for the useful advice on the neutral simulation.

[1] I. Levchenko, S. Xu, G. Teel, D. Mariotti, M. L. R. Walker, and M. Keidar, Nat. Commun. **9**, 879 (2018).
[2] Z. Zhang, W. Y. L. Ling, H. Tang, J. Cao, X. Liu, and N. Wang, Rev. Mod. Plasma Phys. **3**, 5 (2019).
[3] J. J. Szabo, Fully Kinetic Numerical Modeling of a Plasma Thruster (Doctoral dissertation, Massachusetts Institute of Technology), 2001.
[4] Y. Hu and J. Wang, Phys. Rev. E **98**, 023204 (2018).
[5] I. G. Mikellides and I. Katz, Phys. Rev. E **86**, 046703 (2012).
[6] S. Mahalingam and J. A. Menart, J. Propuls. Power **26**, 673 (2010).
[7] C. D. Decker, W. B. Mori, and T. Katsouleas, Phys. Rev. E **50**, R3338 (1994).
[8] Z.-H. Hu, Y.-H. Song, and Y.-N. Wang, Phys. Rev. E **82**, 026404 (2010).
[9] M. H. L. van der Velden, W. J. M. Brok, J. J. A. M. van der Mullen, W. J. Goedheer, and V. Banine, Phys. Rev. E **73**, 036406 (2006).
[10] M. U. U. Hirakawa, Electron transport mechanism in a Hall thruster, in *26th International Electric Propulsion Conference* (Cleveland, Ohio, 1997), pp. 97–021.
[11] S. Cho, K. Komurasaki, and Y. Arakawa, Phys. Plasmas **20**, 063501 (2013).
[12] F. Taccogna, S. Longo, M. Capitelli, and R. Schneider, Phys. Plasmas **12**, 053502 (2005).
[13] H. Liu, B. Wu, D. Yu, Y. Cao, and P. Duan, J. Phys. D: Appl. Phys. **43**, 165202 (2010).
[14] Y. Jiang, H. Tang, J. Ren, M. Li, and J. Cao, J. Phys. D: Appl. Phys. **51**, 035201 (2018).
[15] K. U. Sullivan, PIC Simulation of SPT Hall Thrusters: High Power Operation and Wall Effects (Doctoral dissertation, Massachusetts Institute of Technology), 2004.
[16] Y. Ding, H. Sun, P. Li, L. Wei, H. Su, W. Peng, H. Li, and D. Yu, J. Phys. D: Appl. Phys. **50**, 335201 (2017).
[17] S. Mahalingam, Particle Based Plasma Simulation for An Ion Engine Discharge Chamber, Ph.D. thesis, Wright State University, 2007.
[18] S. Mahalingam, Y. Choi, J. Loverich, P. Stoltz, B. Bias, and J. Menart, in *47th AIAA/ASME/SAE/ASEE Joint Propulsion Conference* (American Institute of Aeronautics and Astronautics, Reston, VA, 2011), pp. 1–24.
[19] J. Cheng, H.-B. Tang, and T. M. York, Phys. Plasmas **21**, 063501 (2014).
[20] M. Li, H.-B. Tang, J.-X. Ren, and T. M. York, Phys. Plasmas **20**, 103502 (2013).

[21] C. K. Birdsall and A. B. Langdon, *Plasma Physics via Computer Simulation* (CRC Press, Boca Raton, FL, 2004).

[22] V. V. Serikov, S. Kawamoto, and K. Nanbu, IEEE Trans. Plasma Sci. **27**, 1389 (1999).

[23] F. Taccogna, R. Schneider, S. Longo, and M. Capitelli, Plasma Sources Sci. Technol. **17**, 024003 (2008).

[24] S. Mahalingam and J. Menart, in *41st AIAA/ASME/SAE/ASEE Joint Propulsion Conference & Exhibit* (American Institute of Aeronautics and Astronautics, Reston, VA, 2005), p. AIAA2005-4254.

[25] J. P. Verboncoeur, A. B. Langdon, and N. T. Gladd, Comput. Phys. Commun. **87**, 199 (1995).

[26] R. Schneider, K. Matyash, O. Kalentev, F. Taccogna, N. Koch, and M. Schirra, Contrib. Plasma Phys. **49**, 655 (2009).

[27] S. Cao, J. Ren, H. Tang, Z. Zhang, Y. Wang, J. Cao, and Z. Chen, Phys. Plasmas **25**, 103512 (2018).

[28] J. C. Adam, A. Héron, and G. Laval, Phys. Plasmas **11**, 295 (2004).

[29] Y. Ding, H. Sun, P. Li, L. Wei, Y. Xu, W. Peng, H. Su, and D. Yu, Vacuum **143**, 251 (2017).

[30] S. J. Araki, in *35th InternationalElectricPropulsionConference*, Atlanta, GA, Oct. 8–12, 2017, pp. 1–12.

[31] I. Katz and I. G. Mikellides, J. Comput. Phys. **230**, 1454 (2011).

[32] C. E. Huerta, T. S. Matlock, and R. E. Wirz, in *AIAA Space 2015 Conference and Exposition* (American Institute of Aeronautics and Astronautics, Reston, VA, 2015), pp. 1–9.

[33] R. E. Wirz, Discharge Plasma Processes of Ring-Cusp Ion Thrusters (Doctoral dissertation, California Institute of Technology), 2005.

[34] H.-S. Mao, Plasma Structure and Behavior of Miniature Ring-cusp Discharges (Doctoral dissertation, UCLA), 2013.

[35] H.-S. Mao, R. E. Wirz, and D. M. Goebel, J. Propuls. Power **30**, 628 (2014).

[36] S. Cao, J. Ren, H. Tang, R. Pan, Z. Zhang, K. Zhang, and J. Cao, J. Phys. D: Appl. Phys. **52**, 285202 (2019).

[37] H.-B. Tang, J. Cheng, C. Liu, and T. M. York, Phys. Plasmas **19**, 073107 (2012).

[38] H.-B. Tang, J. Cheng, C. Liu, and T. M. York, Phys. Plasmas **19**, 073108 (2012).

[39] V. Vahedi and M. Surendra, Comput. Phys. Commun. **87**, 179 (1995).

[40] Y. K. Khor, Y. M. Hung, and B. K. Lim, Int. Commun. Heat Mass Transfer **37**, 1087 (2010).

[41] D. Andrienko, S. Surzhikov, J. J. Shang, and G. P. Huang, in *45th AIAA Plasmadynamics Lasers Conference* (American Institute of Aeronautics and Astronautics, Reston, VA, 2014), pp. 1–17.

[42] D. G. Steyn, Atmos.-Ocean **18**, 254 (1980).

[43] J. S. Miller, S. H. Pullins, D. J. Levandier, Y. Chiu, and R. A. Dressler, J. Appl. Phys. **91**, 984 (2002).

[44] R. Howell, J. Menguc, and M. Siegel, *Thermal Radiation Heat Transfer*, 6th ed. (CRC Press, Boca Raton, FL, 2015).

[45] C. J. Wordingham, P.-Y. Taunay, and E. Choueiri, in *53rd AIAA/SAE/ASEE Joint Propulsion Conference* (American Institute of Aeronautics and Astronautics, Reston, VA, 2017), pp. 1–52.

[46] P. Clausing, J. Vac. Sci. Technol. **8**, 636 (1971).

[47] J. Sturnfield, in *COMSOL Conference2015 Boston*, Newton, MA, 2015.

[48] F. Basirat, P. Sharma, F. Fagerlund, and A. Niemi, Int. J. Greenhouse Gas Control **42**, 461 (2015).

[49] F. Celestini and F. Mortessagne, Phys. Rev. E **77**, 021202 (2008).

[50] D. M. Goebel and I. Katz, *Fundamentals of Electric Propulsion* (John Wiley & Sons, Inc., Hoboken, NJ, 2008), pp. 37–90.

[51] T. Yuan, J. Ren, J. Zhou, Z. Zhang, Y. Wang, and H. Tang, AIP Adv. **10**, 045115 (2020).

[52] D. Levko, Y. E. Krasik, V. Vekselman, and I. Haber, Phys. Plasmas **20**, 083512 (2013).

[53] B. Dankongkakul, Overcoming the Scaling Limitations of Ring-Cusp DC Ion Thruster Discharges (Doctoral dissertation, UCLA), 2017.

[54] B. Dankongkakul and R. E. Wirz, J. Appl. Phys. **122**, 243303 (2017).